Massive Dirac Fermion on the Surface of a Magnetically Doped Topological Insulator

Y. L. Chen,[1,2,3] J.-H. Chu,[1,2] J. G. Analytis,[1,2] Z. K. Liu,[1,2] K. Igarashi,[4] H.-H. Kuo,[1,2] X. L. Qi,[1,2] S. K. Mo,[3] R. G. Moore,[1] D. H. Lu,[1] M. Hashimoto,[2,3] T. Sasagawa,[4] S. C. Zhang,[1,2] I. R. Fisher,[1,2] Z. Hussain,[3] Z. X. Shen[1,2]*

In addition to a bulk energy gap, topological insulators accommodate a conducting, linearly dispersed Dirac surface state. This state is predicted to become massive if time reversal symmetry is broken, and to become insulating if the Fermi energy is positioned inside both the surface and bulk gaps. We introduced magnetic dopants into the three-dimensional topological insulator dibismuth triselenide (Bi_2Se_3) to break the time reversal symmetry and further position the Fermi energy inside the gaps by simultaneous magnetic and charge doping. The resulting insulating massive Dirac fermion state, which we observed by angle-resolved photoemission, paves the way for studying a range of topological phenomena relevant to both condensed matter and particle physics.

Topological insulators are a state of matter that may serve as a platform for both fundamental physics phenomena and technological applications, such as spintronics and quantum information processing. Since their discovery in two-dimensional (2D) HgTe quantum wells (1, 2), topological insulators have been at the core of a very active research area (3–11). Recently, a class of 3D compounds—Bi_2Te_3, Bi_2Se_3, and Sb_2Te_3—were identified (12–14) with the surface state consisting of a single Dirac cone. The conducting surface states of topological insulators are immune to localization as long as the disorder potential does not violate time reversal symmetry (TRS) (4, 5, 9), and one way to destroy this robust surface metallicity is to break the TRS by introducing magnetic order (5). In the bulk, a topological insulator doped with magnetic impurities can have a long-range magnetic order both in the metallic (15, 16) and insulating (17) phases; on the surface, such a long-range magnetic order can also be formed independent of the bulk magnetic ordering, as the Ruderman-Kittel-Kasuya-Yosida (RKKY) interaction induced by the Dirac fermions is generally ferromagnetic when the Fermi energy (E_F) is close to the Dirac point (18). Both effects can lead to the breaking of TRS, resulting in a gap opening at the Dirac point that makes the surface Dirac fermion mas-

[1]Stanford Institute for Materials and Energy Sciences, SLAC National Accelerator Laboratory, 2575 Sand Hill Road, Menlo Park, CA 94025, USA. [2]Geballe Laboratory for Advanced Materials, Departments of Physics and Applied Physics, Stanford University, Stanford, CA 94305, USA. [3]Advanced Light Source, Lawrence Berkeley National Laboratory, Berkeley, CA 94720, USA. [4]Materials and Structures Laboratory, Tokyo Institute of Technology, Kanagawa 226-8503, Japan.

*To whom correspondence should be addressed. E-mail: zxshen@stanford.edu

Fig. 1. Electronic band structure of undoped Bi_2Se_3 measured by ARPES. (**A**) The bulk conduction band (BCB), bulk valence band (BVB), and surface-state band (SSB) are indicated, along with the Fermi energy (E_F), the bottom of the BCB (E_B), and the Dirac point (E_D). (**B**) Constant-energy contours of the band structure show the SSB evolution from the Dirac point to a hexagonal shape (green dashed lines). (**C**) Band structure along the K-Γ-K direction, where Γ is the center of the hexagonal surface Brillouin zone (BZ), and the K and M points [see (D)] are the vertex and the midpoint of the side of the BZ, respectively (14). The BCB bottom is ~190 meV above E_D and 150 meV below E_F. (**D**) Photon energy–dependent FS maps (symmetrized according to the crystal symmetry). Blue dashed lines around the BCB FS pocket indicate their different shapes.
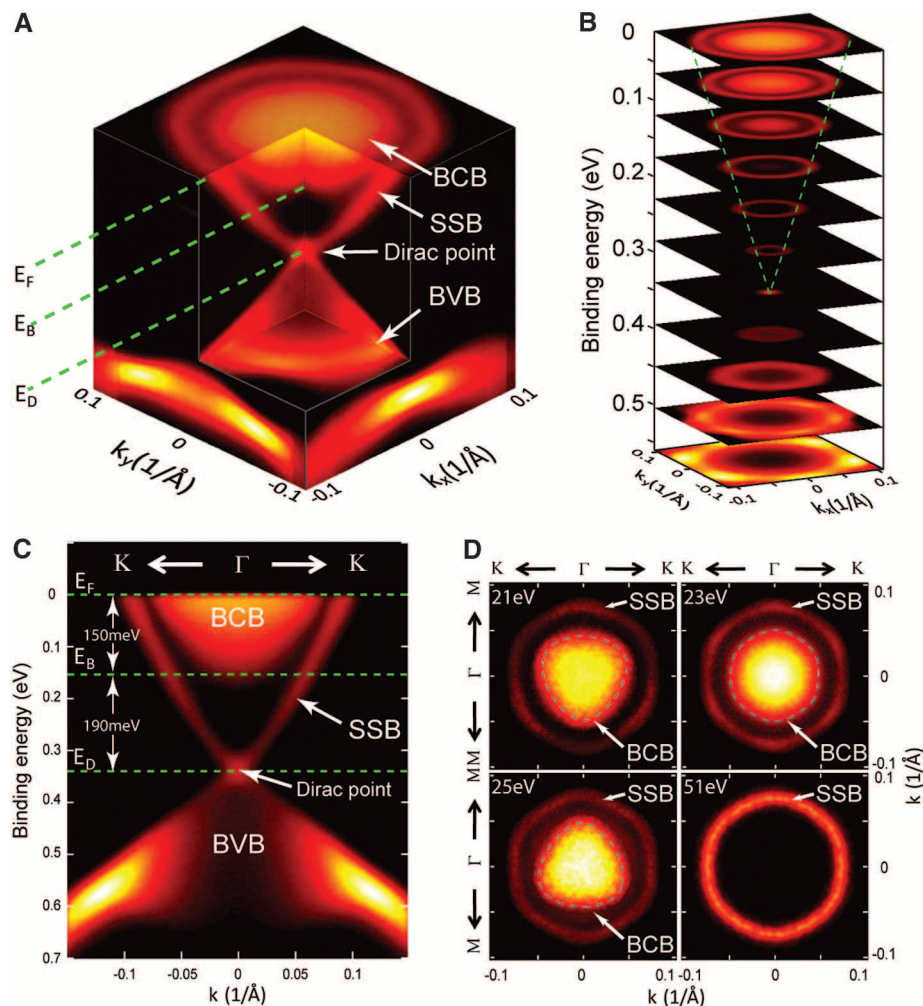
sive; indeed, we find that the Dirac gap can be observed in magnetically doped samples with or without bulk ferromagnetism (19). Furthermore, if E_F can be tuned into this surface-state gap, an insulating massive Dirac fermion state is formed; this state may support many striking topological phenomena, such as the image magnetic mono-

pole induced by a point charge (20, 21), the half quantum Hall effect on the surface with a Hall conductance of $e^2/2h$, and a topological contribution to the Faraday and Kerr effects (5). In addition, this state is a concrete realization of the "θ vacuum" state of axion physics in a condensed matter system (5), and thus has implications for

particle physics and cosmology (22). Finally, a tunable energy gap at the surface Dirac point provides a means to control the surface electric transport, which is of great importance for applications.

The insulating massive Dirac fermion state is challenging to realize, because there are two critical requirements that must be simultaneously
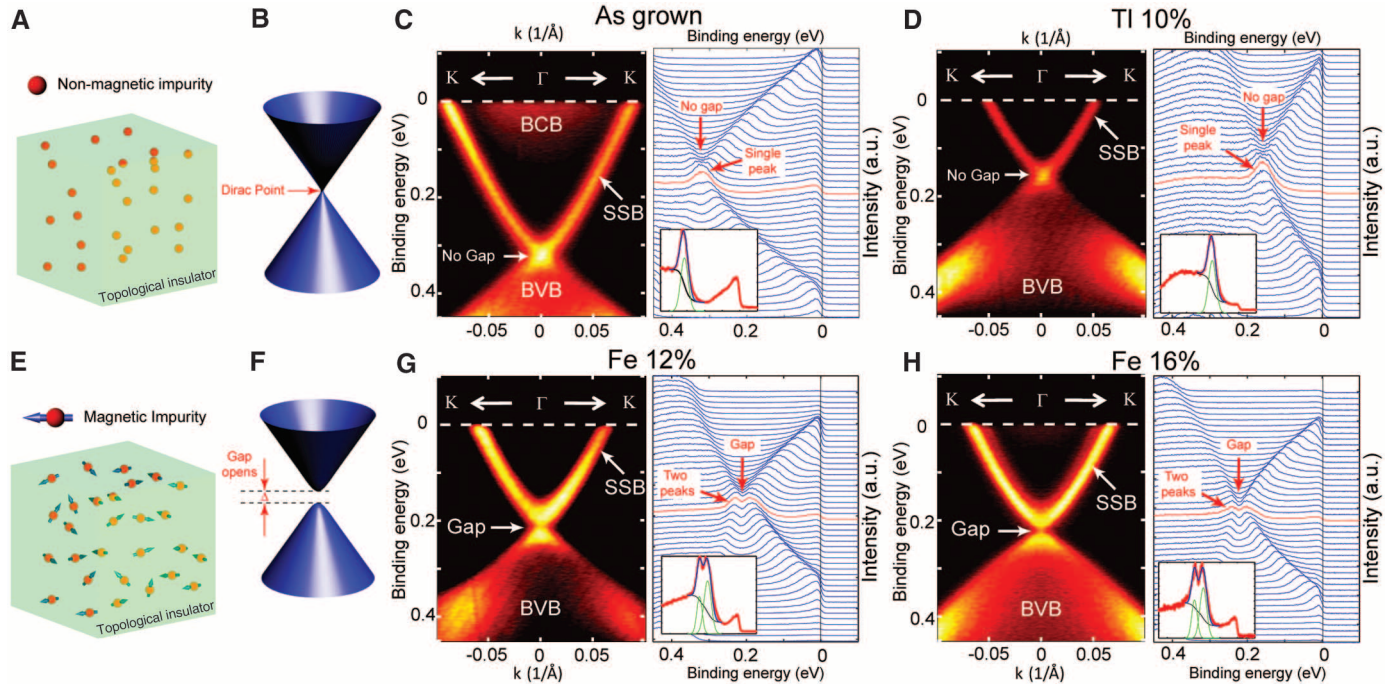

Fig. 2. (**A** and **B**) A nonmagnetically doped topological insulator with a Dirac point connecting the upper and lower Dirac cones as in the undoped case. (**C**) Band structure along the K-Γ-K direction of undoped Bi_2Se_3. Left and right subpanels show the ARPES spectral intensity plot and a stacking plot of the energy distribution curves (EDCs), respectively. The red curve in the right subpanel indicates the EDC at the Γ point. Inset: EDC at the Γ point (red), fitted with a Lorentzian peak (green) on the Shirley background (black); the total fitting function is shown in blue. The same convention is used in (D), (G), and (H). (**D**) Band structure for a Tl-doped sample, $(Bi_{0.9}Tl_{0.1})_2Se_3$. The Dirac point remains continuous. (**E** and **F**) A magnetically doped topological insulator with a broken Dirac point and a gap separating the upper and lower Dirac cones. (**G** and **H**) Band structure of two Fe-doped samples from two growth batches with melt composition $(Bi_{0.88}Fe_{0.12})_2Se_{3.7}$ and $(Bi_{0.84}Fe_{0.16})_2Se_{3.7}$, respectively. At the Dirac point, the reduced spectral intensity (left subpanels) and the twin-peak structure in the EDCs (right subpanels) indicate a gap formation.

Fig. 3. Realization of the insulating massive Dirac fermion state by simultaneous magnetic and charge doping. (**A**) Gap formation at the Dirac point (caused by magnetic impurities on the surface) and the in-gap E_F position. The occupied and unoccupied Dirac cones are shown in blue and gray, respectively; Δ is the energy difference between the top of the occupied Dirac cone and E_F. (**B**) ARPES spectra intensity plot of the band structure along the K-Γ-K direction of Mn-doped sample $(Bi_{0.99}Mn_{0.01})_2Se_3$ showing the E_F inside the surface Dirac gap. Inset: close-up of the dispersion in the vicinity of E_F, indicating a gap between the leading edge of the SSB and E_F. Vertical white dashed line shows the location of the EDC plotted in (C). (**C**) Comparison between the Γ point EDC (blue) and E_F shows a leading-edge gap of 7 meV (EDC on the full energy scale is plotted in the inset). A reference EDC from a polycrystalline Au sample whose leading edge, as expected, coincides with E_F is shown in red.
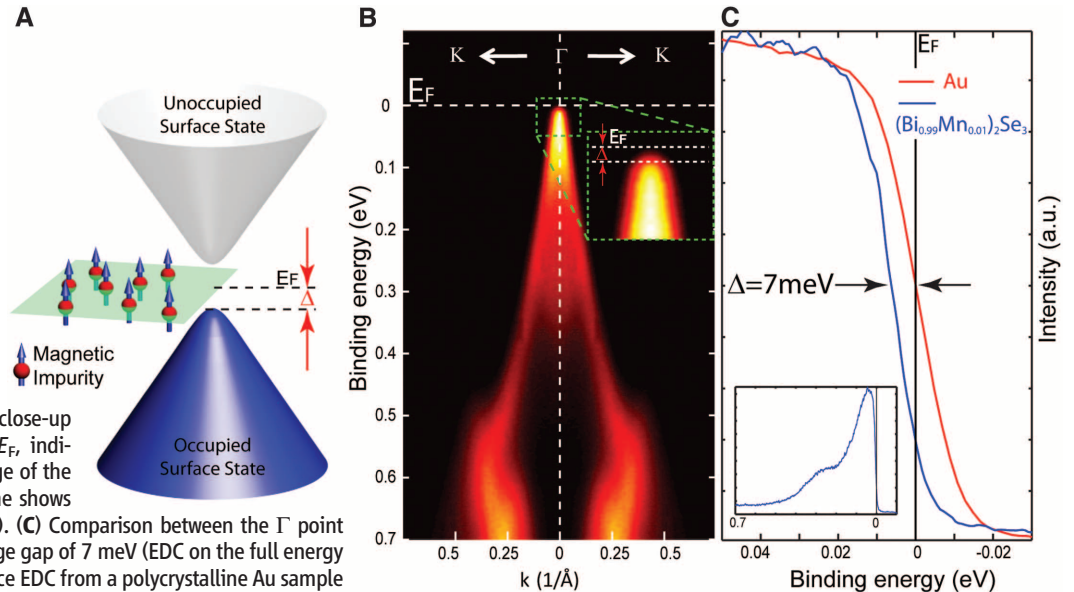
satisfied: (i) A gap should open at the Dirac point of the topological surface state (as a result of the breaking of TRS); (ii) the E_F of the system must reside inside both the surface and bulk gaps. We report the realization of this state with simultaneous fulfillment of both requirements in the topological insulator Bi_2Se_3 by introducing an exact amount of magnetic dopants to break the TRS and precisely controlling the E_F position.

We performed angle-resolved photoemission spectroscopy (ARPES) to investigate the electronic structures of intrinsic, nonmagnetically doped, and magnetically doped Bi_2Se_3 (19). Figure 1 illustrates the measured band structure of undoped Bi_2Se_3. Similar to Bi_2Te_3 (14), besides the Fermi surface (FS) pocket from the surface-state band (SSB), there is also a FS pocket from the bulk conduction band (BCB) (Fig. 1, A to D) due to the Se deficiencies and the Bi-Se intersite defects. The bottom of the BCB is located at 190 meV above the Dirac point (Fig. 1, A and C), indicating a direct bulk gap (19). The in-gap Dirac point makes Bi_2Se_3 a better candidate for realizing the insulating massive Dirac fermion state than Bi_2Te_3, in which the Dirac point is below the top

of the bulk valence band (BVB) (14), thus demanding a much larger surface energy gap for E_F to reside inside both the surface and bulk gaps. The cross-sectional plot of the band structure (Fig. 1B) shows how the SSB evolves from the Dirac point to a hexagonal shape at E_F. Unlike the Bi_2Te_3 band structure, where the SSB FS starts being warped at energies close to the BCB minimum (14) and becomes a concave hexagram, the SSB FS of Bi_2Se_3 remains convex hexagonal even in the presence of the BCB. This difference will be reflected in other experiments, such as scanning tunneling microscopy/spectroscopy (STM/STS), where the surface quasi-particle interference around defects can be suppressed in Bi_2Se_3 but not in Bi_2Te_3, where the concave SSB FS shape favors such scattering along specific directions (23–27).

The surface nature of the hexagonal SSB FS was confirmed by the photon energy–dependent ARPES (Fig. 1D), where its nonvarying shape with different excitation photon energies indicates its 2D nature. By contrast, the shape and the existence of the inner BCB FS pocket changes markedly because of its 3D nature with strong k_z dispersion.

In the presence of TRS, the SSB of Bi_2Se_3 is degenerate at the Dirac point, which connects the upper- and lower-surface Dirac cone (Fig. 2B) even if the system is perturbed by nonmagnetic dopants (Fig. 2A). This is confirmed by the ARPES measurements (Fig. 2, C and D), where the band structures of an intrinsic sample and a nominally 10% Tl-doped sample are shown, respectively. In both cases, the continuity at the Dirac point is indicated by the strong spectral intensity (left subpanels) and the single-peak structure of the energy distribution curve (EDC) at the Dirac point (right subpanels). In Fig. 2D, the charge doping effect of Tl is clearly shown by the marked shift of E_F into the bulk gap ($E_F - E_D = 160$ meV). Nonetheless, the topology of the SSB remains the same with a continuous Dirac point (19).

The TRS protection of the Dirac point can be lifted by magnetic dopants (Fig. 2E), resulting in a gap that separates the upper and lower branches of the Dirac cone (Fig. 2F). This is illustrated in the band structure (Fig. 2, G and H) of two Fe-doped samples. Unlike nonmagnetically doped samples, for both Fe-doped samples, the SSB dispersion at the Dirac point is broken, as indicated by the suppressed intensity regions in the spectral density plots (left subpanels) and the twin-peak structure around the Dirac point in the EDC plots (right subpanels). The data have sufficient k-space sampling density to reveal the qualitative difference between the nonmagnetic and magnetic dopants: One always finds a single-peak structure in as-grown and nonmagnetically doped samples, whereas the twin-peak structure is present only in magnetically doped samples (19). By fitting the twin-peak structure with two Lorentzian peaks (insets in EDC plots of Fig. 2, G and H), the gap size can be acquired, showing a larger value (~50 meV) in Fig. 2H than that (~44 meV) in Fig. 2G. This trend (19) is consistent with the increase of the magnetic moment upon increasing the magnetic dopant concentration.

The SSB gap formation at the Dirac point with broken TRS is the first step in realizing the insulating massive Dirac fermion state; the second step is to tune the E_F into this gap. In the Fe-doped Bi_2Se_3, however, E_F was found to always reside above the Dirac point (similar to undoped Bi_2Se_3), making the material n-type (Fig. 2, G and H). To remove these excess n-type carriers while maintaining the magnetic doping effect, we changed the dopant from Fe to Mn, another magnetic material with one less valence electron than Fe. Indeed, Mn dopants not only introduce magnetic moments into the system, but also naturally p-dope the samples. The measurements on an optimally doped sample (19) show E_F residing just inside the SSB gap (Fig. 3B). By comparing the leading edge of the EDC at the Γ point to E_F (Fig. 3C; also shown is an Au reference spectrum), we found a 7-meV difference, indicating a SSB Dirac gap of at least 7 meV (Fig. 3A). Such a gap suggests a ferromagnetic order of the Mn dopants on the surface, which can be induced by the ferromagnetic spin-spin interaction mediated by the
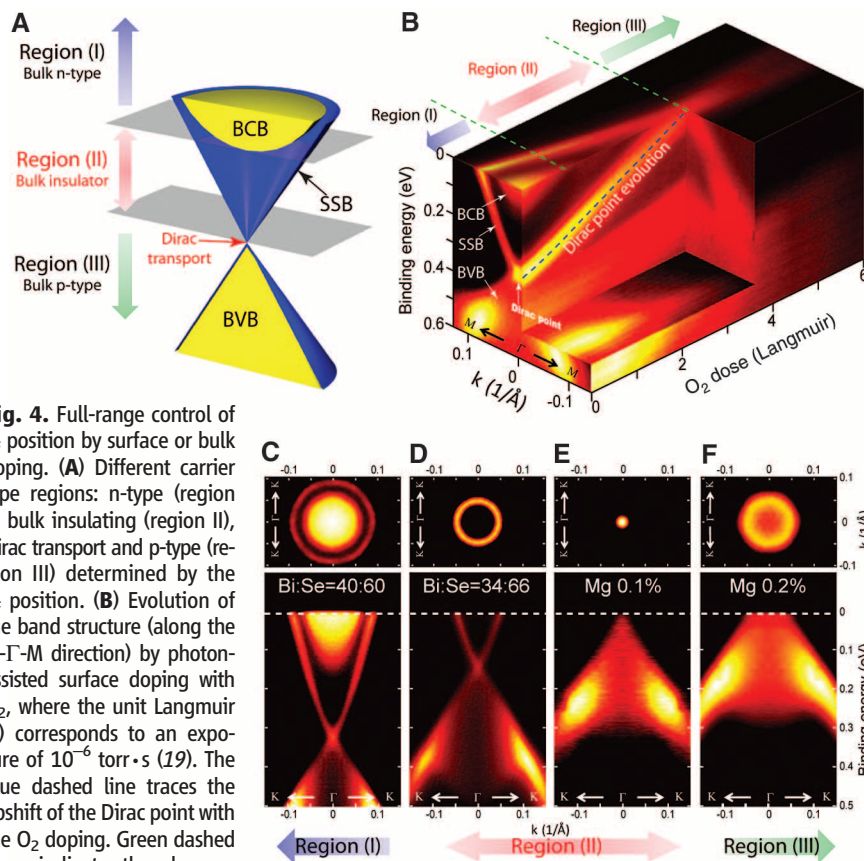

Fig. 4. Full-range control of E_F position by surface or bulk doping. (**A**) Different carrier type regions: n-type (region I), bulk insulating (region II), Dirac transport and p-type (region III) determined by the E_F position. (**B**) Evolution of the band structure (along the M-Γ-M direction) by photon-assisted surface doping with O_2, where the unit Langmuir (L) corresponds to an exposure of 10^{-6} torr·s (19). The blue dashed line traces the upshift of the Dirac point with the O_2 doping. Green dashed lines indicate the dosages that separate the three doping regions shown in (A): At 0.95L O_2 dosage, the BCB bottom reaches E_F; at 3.6L, the Dirac point reaches E_F; and beyond 3.6L, the Dirac point is above E_F. (**C** to **F**) Bulk doping: the FS and the band structure of (C) nominally undoped Bi_2Se_3, showing the coexistence of BCB and SSB FS pockets; (D) Se-rich sample (melt composition $Bi_{1.7}Se_{3.3}$) with only an SSB FS, and E_F residing inside the bulk gap ($E_F - E_D = 145$ meV); (E) Mg-doped ($Bi_{0.999}Mg_{0.001})_2Se_3$ sample with a point-like FS and E_F precisely at the Dirac point; and (F) more richly Mg-doped ($Bi_{0.998}Mg_{0.002})_2Se_3$ sample driven into p-type, with a p-type FS and the Dirac point above E_F.

surface states (*18*). This optimally doped sample thus fully realizes the insulating massive Dirac fermion state and provides a model system for studying striking topological phenomena (*5, 20–22*).

To maintain this insulating massive Dirac fermion state at higher temperatures requires a further increase of the Dirac gap (while keeping E_F inside it). However, because of the hole-doping effect of Mn dopants, one cannot simply increase the Mn concentration in $(Bi_{1-\delta}Mn_\delta)_2Se_3$ to acquire a larger Dirac gap, as the system will become p-type before the gap magnitude increases appreciably (*19*). However, we found that it was possible to introduce many Fe dopants into Bi_2Se_3 to increase the gap size without substantially altering the E_F position relative to the undoped Bi_2Se_3; if we can then move E_F into the gap by introducing additional p-type dopants, we can achieve a larger gap while preserving the insulating nature of the state.

Figure 4 demonstrates the full range of E_F tuning by introducing such p-type doping, with three doping regions and the topological transport point (where E_F coincides with the Dirac point) shown in Fig. 4A. By either surface doping [Fig. 4B and (*19*)] or bulk doping (Fig. 4, C to F), we were able to tune the E_F to any of the regions defined in Fig. 4A. The ability to convert the original n-type sample to p-type by surface doping (Fig. 4B, region III) is critical for applications requiring both types of carriers or p-n junctions. On the other hand, full-range bulk doping (Fig. 4, C to F) has advantages over surface doping in bulk applications.

References and Notes

1. B. A. Bernevig, T. L. Hughes, S.-C. Zhang, *Science* **314**, 1757 (2006).
2. M. König et al., *Science* **318**, 766 (2007); published online 20 September 2007 (10.1126/science.1148047).
3. X. L. Qi, S. C. Zhang, *Phys. Today* **63**, 33 (2010).
4. L. Fu, C. L. Kane, E. J. Mele, *Phys. Rev. Lett.* **98**, 106803 (2007).
5. X. L. Qi, T. L. Hughes, S. C. Zhang, *Phys. Rev. B* **78**, 195424 (2008).
6. A. P. Schnyder, S. Ryu, A. Furusaki, A. W. Ludwig, *Phys. Rev. B* **78**, 195125 (2008).
7. L. Fu, C. L. Kane, *Phys. Rev. Lett.* **102**, 216403 (2009).
8. A. R. Akhmerov, J. Nilsson, C. W. J. Beenakker, *Phys. Rev. Lett.* **102**, 216404 (2009).
9. J. E. Moore, L. Balents, *Phys. Rev. B* **75**, 121306(R) (2007).
10. R. Roy, *Phys. Rev. B* **79**, 195321 (2009).
11. B. Seradjeh, J. E. Moore, M. Franz, *Phys. Rev. Lett.* **103**, 066402 (2009).
12. H. Zhang et al., *Nat. Phys.* **5**, 438 (2009).
13. Y. Xia et al., *Nat. Phys.* **5**, 398 (2009).
14. Y. L. Chen et al., *Science* **325**, 178 (2009); published online 11 June 2009 (10.1126/science.1173034).
15. J. Choi et al., *Phys. Status Solidi B* **241**, 1541 (2004).
16. Y. S. Hor et al., *Phys. Rev. B* **81**, 195203 (2010).
17. R. Yu et al., *Science* **329**, 61 (2010); published online 3 June 2010 (10.1126/science.1187485).
18. Q. Liu, C. X. Liu, C. K. Xu, X. L. Qi, S. C. Zhang, *Phys. Rev. Lett.* **102**, 156603 (2009).
19. See supporting material on *Science* Online.
20. X.-L. Qi, R. Li, J. Zang, S.-C. Zhang, *Science* **323**, 1184 (2009); published online 29 January 2009 (10.1126/science.1167747).
21. J. Zang, N. Nagaosa, *Phys. Rev. B* **81**, 245125 (2010).
22. F. Wilczek, *Nature* **458**, 129 (2009).
23. L. Fu, *Phys. Rev. Lett.* **103**, 266801 (2009).
24. X. Zhou, C. Fang, W. F. Tsai, J. P. Hu, *Phys. Rev. B* **80**, 245317 (2009).
25. W. C. Lee, C. Wu, D. P. Arovas, S. C. Zhang, *Phys. Rev. B* **80**, 245439 (2009).
26. Z. Alpichshev et al., *Phys. Rev. Lett.* **104**, 016401 (2010).
27. T. Zhang et al., http://arxiv.org/abs/0908.4136 (2009).
28. Supported by the Department of Energy, Office of Basic Energy Science, under contract DE-AC02-76SF00515.

Quantum Correlations in Optical Angle–Orbital Angular Momentum Variables

Jonathan Leach,[1] Barry Jack,[1] Jacqui Romero,[1] Anand K. Jha,[2] Alison M. Yao,[3] Sonja Franke-Arnold,[1] David G. Ireland,[1] Robert W. Boyd,[2] Stephen M. Barnett,[3] Miles J. Padgett[1]*

Entanglement of the properties of two separated particles constitutes a fundamental signature of quantum mechanics and is a key resource for quantum information science. We demonstrate strong Einstein, Podolsky, and Rosen correlations between the angular position and orbital angular momentum of two photons created by the nonlinear optical process of spontaneous parametric down-conversion. The discrete nature of orbital angular momentum and the continuous but periodic nature of angular position give rise to a special sort of entanglement between these two variables. The resulting correlations are found to be an order of magnitude stronger than those allowed by the uncertainty principle for independent (nonentangled) particles. Our results suggest that angular position and orbital angular momentum may find important applications in quantum information science.

In 1935, Einstein, Podolsky, and Rosen (EPR) proposed a Gedanken experiment that was intended to show that quantum mechanics is incomplete (*1*). Their proposal supposes the existence of two spatially separated particles that are perfectly correlated in both position and momentum. Measurement of the position (or alternatively the momentum) of one particle would then determine instantaneously the position (or momentum) of the second particle. The ability to infer either the position or the momentum of the second particle from a distant measurement on the first seems to imply that both of these quantities must have been predetermined. However, quantum theory (and specifically the uncertainty principle) does not allow the simultaneous, exact knowledge of two noncommuting observables, such as position and momentum, as seems to be required for the second particle. A demonstration of EPR correlations establishes either that quantum mechanics is incomplete, in that systems possess additional hidden variables, or that quantum mechanics is nonlocal, in that measurement of the position or momentum of either particle results in an instantaneous uncertainty of the momentum or position, respectively, of both (*2*).

In 1964, Bell deduced an inequality that distinguishes the predictions of quantum theory from those of any local hidden variable theory (*3, 4*). Since that time, many experiments have been performed that have decided strongly in favor of quantum theory (*5, 6*). These Bell-type tests apply only to discrete state-spaces, originally of two dimensions or, more recently, to three or higher dimensions (*7–9*). In contrast, EPR correlations provide a demonstration of entanglement both for discrete and continuous variables, such as energy and time (*10*), position and linear momentum (*11*), spatial modes (*12, 13*), and images (*14*).

In addition to linear momentum, light may also carry angular momentum. The spin angular momentum is manifest as the polarization of light and is described completely within a two-dimensional Hilbert space. However, light beams can also carry a measurable orbital angular momentum that results from their helical phase structure. This phase structure can be described by $\exp(i\ell\phi)$(*15, 16*), where ϕ is the azimuthal angle and ℓ can take any integer value, corresponding to an orbital angular momentum in the direction of propagation of $L_z = \ell\hbar$ per photon, where $\hbar$ is Planck's constant h divided by 2π. For restricted subspaces of two or three dimensions, the orbital angular momentum variable has previously been shown to be an entangled property of down-converted photon pairs (*17, 18*) and to violate a

[1]Department of Physics and Astronomy, Scottish Universities Physics Alliance (SUPA), University of Glasgow, Glasgow, G12 8QQ, UK. [2]Institute of Optics, University of Rochester, Rochester, NY 14627, USA. [3]Department of Physics, SUPA, University of Strathclyde, Glasgow, G4 0NG, UK.

*To whom correspondence should be addressed. E-mail: m.padgett@physics.gla.ac.uk